Coexistence of topological nodal lines, Weyl points, and triply degenerate points in TaS

Jian-Peng Sun, Dong Zhang,* and Kai Chang†
SKLSM, Institute of Semiconductors, Chinese Academy of Sciences, P.O. Box 912, 100083 Beijing, China
(Received 14 March 2017; published 17 July 2017)

We theoretically propose that the single-crystal formed TaS is a new type of topological metal, hosting ring-shaped gapless nodal lines and triply degenerate points (TDPs) in the absence of spin-orbit coupling (SOC). In the presence of SOC, each TDP splits into four TDPs along the high-symmetric line in momentum space, and one of the nodal rings remains closed due to the protection of the mirror reflection symmetry, while another nodal ring is fully gapped and transforms into six pairs of Weyl points (WPs) carrying opposite chirality. The electronic structures of the projected surfaces are also discussed, the unique Fermi arcs are observed, and the chirality remains or vanishes depending on the projection directions. On the (010) projected surface, one may observe a Lifshitz transition. The new type of topological metal TaS is stable and experimentally achievable, and the coexistence of topological nodal lines, WPs, and TDPs in TaS makes it a potential candidate to study the interplay between different types of topological fermions.

DOI: 10.1103/PhysRevB.96.045121

I. INTRODUCTION

Topological semimetals (TSMs) have stimulated tremendous interest in recent years, not only because they metallically mimic topological insulators [1–4] but also because they provide fertile platforms to realize unique particles in high-energy particle physics. The search for novel fermions in condensed matter stems back to 1937 [5], when Herring proposed accidental twofold degeneracy of bands crossing in a three-dimensional (3D) lattice and found it robust even without any symmetry protection within the Weyl function. Later, Volovik proposed Weyl fermions in superfluid ^{3}He-A [6]. In 2011, Wan *et al.* proposed the first specific compound $Re_2Ir_2O_7$ (Re = rare-earth element) [7] to be a Weyl semimetal. After that, abundant TSM candidates have been proposed.

Current TSMs can be classified as Weyl semimetals, Dirac semimetals, and node-line semimetals according to the different band crossing points at the Fermi level and the mechanisms protecting them. To be more specific, a Dirac semimetal [8–11] is characterized by hosting Dirac points of linear crossing of two doubly degenerate bands in momentum space near the Fermi level. The Dirac points are protected by certain crystalline symmetry, as a result, which makes the quadruple degenerate points located either at the high-symmetry point or along high-symmetry lines. The node-line semimetal [12–23] is another type of TSM where the valence and conduction bands cross along one-dimensional (1D) lines in momentum space, which results in forming a ring-shaped nodal line. Different from the Dirac and node-line semimetals, the Weyl semimetal [7,24–32] is classified by possessing Weyl points (WPs) that are pointlike band crossings of two nondegenerate bands with linear dispersion near the Fermi level. A Weyl semimetal does not require any protection from the crystalline symmetry other than lattice translation, which makes WPs possibly located at generic **k** points. These WPs with opposite chirality represent sources or sinks of Berry curvature and have to appear in pairs. They are associated with the topological Chern number $\mathcal{C} = \pm 1$ and positive (negative) Chern number is equivalent to a source (sink) of Berry curvature. Both Weyl and Dirac semimetals possess Fermi surfaces consisting of a few crossing points in the Brillouin zone (BZ). However, the Fermi surface of a node-line semimetal is a closed ring-shaped nodal line arising from the valence and conduction bands crossing along the specific crystallographic orientations in the BZ.

Besides the above-mentioned topological semimetals, another class of topological semimetal materials characterized by three- or sixfold band crossings has been proposed and is named as "new fermion" by Bradlyn *et al.* [33]. Very recently, the TSMs with triply degenerate points (TDPs) have been predicted theoretically in some materials with hexagonal lattice structure [34,35] and the CuPt-ordered alloys $InAs_{0.5}Sb_{0.5}$ [36]. In the band structures of these materials, both one- and two-dimensional representations are allowed along a certain high-symmetry axis, which makes it possible to generate band crossing between a doubly degenerate band and a nondegenerate band near the Fermi level and form a TDP [37]. This new type of three-component fermions can be regarded as the "intermediate state" between the four-component Dirac and the two-component Weyl fermions.

As the new fermions emerge, the interplay among the fermions reveals underlying physics. For example, the Dirac fermions can split into one pair of Weyl fermions with opposite chirality by breaking spatial inversion or time-reversal symmetry [11,38], and the ring-shaped nodal lines can be gapped [21,22] or split into Weyl fermions [26,35]. From this point of view, hunting for materials hosting versatile topological particles is of particular interest.

In this paper, we propose that TaS is a new type of material that hosts topological nodal lines, Weyl fermion states, and unique fermion states with triply degenerate crossing points near the Fermi level simultaneously. There will be six pairs of WPs near the mirror plane $k_z = 0$. Every pair of WPs possesses opposite chirality (+1 or −1) and each WP can be viewed as a singular point of Berry curvature or "magnetic monopole" in momentum space [7]. Since TaS owns unique D_{3h} symmetry, all WPs are located at the same energy. Along the $\Gamma - A$ line in the BZ, four TDPs are presented in the vicinity of the Fermi energy. These TDPs are protected by the C_3 rotation symmetry along the $\Gamma - A$ direction. The

*zhangdong@semi.ac.cn
†kchang@semi.ac.cn

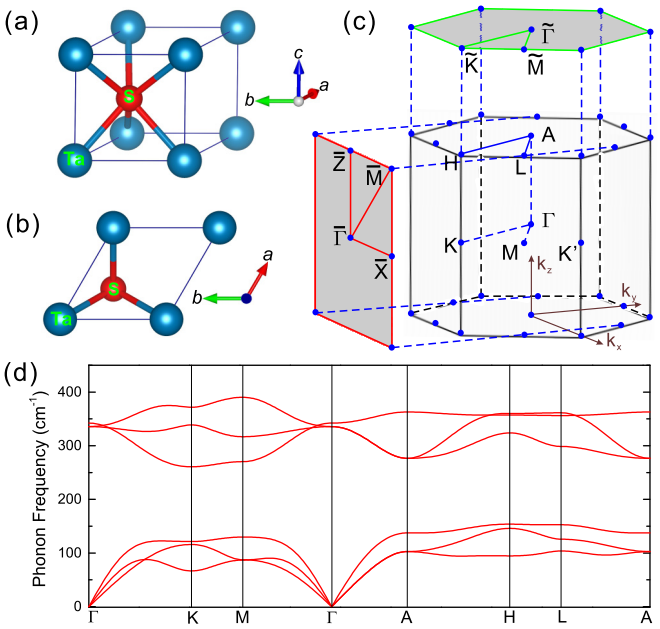

FIG. 1. The overview (a) and top view (b) of the unit cell of the TaS single crystal. (c) The bulk Brillouin zone and its projection onto the (001) and (010) surfaces. (d) The phonon dispersion curves for TaS.

coexistence of topological nodal lines, WPs, and TDPs in TaS makes it a potential candidate to study the interplay between different types of topological fermions.

II. MODELS AND METHODS

As shown in Fig. 1, TaS has a hexagonal lattice structure [39], the same as Ta(Nb)N [40–42] and ZrTe [43], which host the same symmetry D_{3h}^1 with space group $P\bar{6}m2$ (No. 187). Ta and S atoms are located in $1a(0,0,0)$ and $1d(\frac{1}{3},\frac{2}{3},\frac{1}{2})$ Wyckoff positions, respectively. The optimized lattice constants are $a = b = 3.273$ Å and $c = 3.337$ Å, which reasonably agree with experimental data $a = b = 3.280$ Å and $c = 3.145$ Å. To further prove the structural stability of the optimized crystal, we calculate the phonon dispersions by using the frozen phonon method [44] as implemented in the PHONOPY code [45], as shown in Fig. 1(d). No imaginary frequencies are observed throughout the whole BZ in phonon dispersions, indicating its dynamically structural stability. Therefore, in this paper, we adopt the relaxed lattice parameters for all the consequential calculations.

To explore the electronic structures of TaS, we perform the band-structure calculation by using the Vienna *ab initio* simulation package [46] within the generalized gradient approximation in the Perdew-Burke-Ernzerhof [47] type and the projector augmented-wave pseudopotential [48]. The kinetic-energy cutoff is set to be 560 eV for wave-function expansion, and the k-point grid is sampled by sums over $12 \times 12 \times 12$ [49]. For the convergence of the electronic self-consistent calculations, the total energy difference criterion is set to 10^{-8} eV. The crystal structure is fully relaxed until the residual forces on atoms are less than 0.01 eV/Å. In order to investigate the projected surface states and Fermi surfaces, a tight-binding model Hamiltonian based on the maximally localized Wannier function (MLWF) method [50,51] has been constructed. Then, we apply an iterative method [52,53] implemented in the software package WANNIERTOOLS [54] to obtain the surface Green's function of the semi-infinite system and the imaginary part of the surface Green's function is the local density of states at the surface.

III. RESULTS AND DISCUSSIONS

A. Overview of electronic structures of the bulk material

Since each transition-metal Ta connects to six S atoms with an oxidation state +2 within the unit cell, the d electron configuration should be d^3. Further spin-polarized calculation confirms the material shows no magnetism. From Fig. 2(a), one can capture the idea that, near the Fermi level, the valence and conduction bands are mainly attributed to the d orbitals of Ta. In the absence of SOC, there is a band inversion around the K point between $d_{x^2-y^2} + d_{xy}$ and $d_{xz} + d_{yz}$ of the Ta atom, which leads to a gapless nodal ring centering at the K point in the horizontal $k_z = 0$ mirror plane protected by σ_h symmetry. The similar nodal ring band topology is observed in ZrTe [34,35] and MoC [23], but is missing in TaN [34]. Since the three materials share the same space group with TaS, the existence of the nodal ring is not simply determined by the crystal symmetry. Unlike the character of inverted band structures around the K point, we find a band crossing between one nondegenerate band composed by the d_{z^2} orbital of the Ta atom and a doubly degenerate band composed by the combination of $d_{x^2-y^2}$ and d_{xy} orbitals of the Ta atom along the $\Gamma - A$ line in the reciprocal lattice. The crossing point is a TDP protected by the C_{3v} symmetry in the absence of SOC. Since TaS hosts the heavy element Ta, the SOC cannot be simply ignored. By introducing the SOC, due to the lack of inversion symmetry, the energy bands happen to split in momentum space, as demonstrated in Fig. 2(b). From Fig. 2(b), one can find out that the nodal ring centering at the K point is gapped and the original TDP splits into four discrete crossing points along the $\Gamma - A$ symmetric line. Considering that the electronic structures within the $k_z = 0$ and π planes can be decoupled and regarded as individual 2D subsystems with time-reversal symmetry, we can give a well-defined $\mathbb{Z}_2$ number to determine the band topology for all the occupied bands. Since TaS has no inversion symmetry, we use the method of the evolution of Wannier charge centers (WCCs) [55–57] to calculate the $\mathbb{Z}_2$ number by counting how many times the evolution lines of the Wannier centers cross an arbitrary reference line. In Figs. 2(c) and 2(d), we find that both $k_z = 0$ and π planes are topologically nontrivial with $\mathbb{Z}_2 = 1$.

B. Nodal lines and triply degenerate points

In order to understand the role of SOC in the nodal ring gapping and TDP splitting, we calculated the detailed band structures of TaS in the absence and presence of SOC within specific BZ regions.

The enlarged band structures around the K and H points are shown in Fig. 3. In the absence of SOC, there are two nodal lines appearing on the mirror plane of $k_z = 0$ and π, respectively. The nodal line on the $k_z = 0$ plane is located about

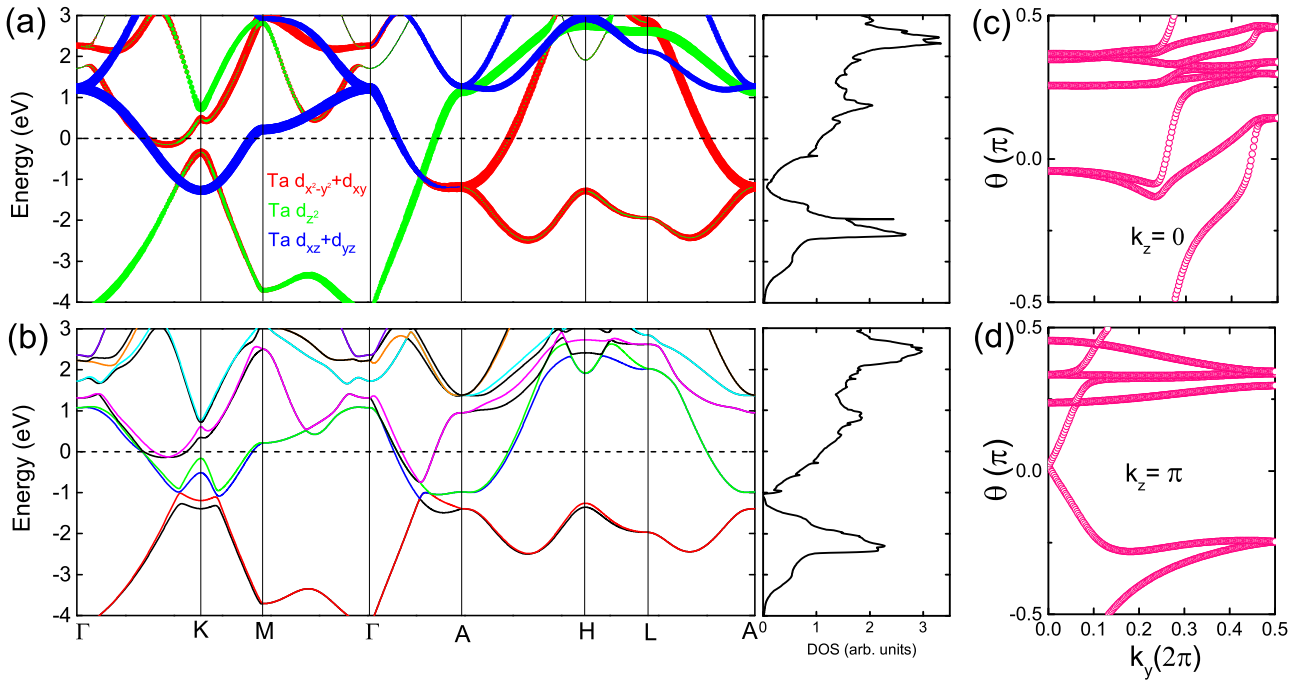

FIG. 2. Band structures and density of states (DOS) of TaS without (a) and with (b) the inclusion of SOC. The pink circles denote the evolution of Wannier centers for TaS along k_y in the (c) $k_z = 0$ and (d) $k_z = \pi$ planes.

1.1 eV below the Fermi level centering at the K point, while the other one on the $k_z = \pi$ plane is located about 2.8 eV above the Fermi level centering at the H point, as shown in Figs. 3(a) and 3(c). By turning on the SOC, the nodal ring around the K point is fully gapped, as shown in Fig. 3(b). However, different from the K point, the nodal ring around the H point still preserves and splits into two nodal rings marked by red and blue dots, respectively, in Fig. 3(d) in the presence of SOC. The preserving of the nodal ring under SOC is strictly protected by the mirror symmetry σ_h. Along the $\Gamma - A$ direction, there are four triply degenerate crossing points emerging near the Fermi level due to the band splitting induced by SOC, as shown in Fig. 4. Due to the the time-reversal symmetry, these TDPs appear in pairs and are protected by threefold rotation symmetry C_3 and vertical mirror symmetry σ_v. The four TDPs located within a relatively large energy scale ranging from -1.141 to 0.812 eV are a direct result stemming from the large SOC in the heavy element Ta. For a more direct view of the degeneracy and separation of energy bands, the 3D Fermi surface at $E = 0$ eV is presented in Fig. 4(c).

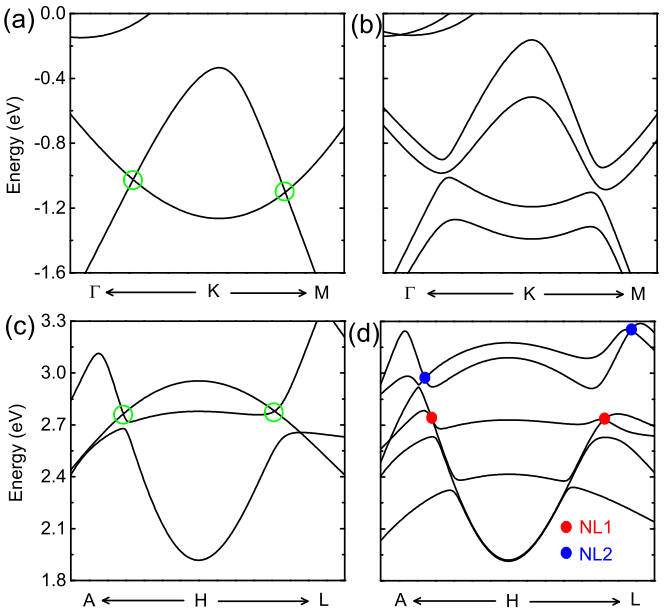

FIG. 3. Band structures around the K point in the absence of (a) and presence of (b) SOC. Band structures around the H point in the absence of (c) and presence of (d) SOC. In the panels, the locations of the ring-shaped nodal lines are indicated by the green circles and red (NL1) and blue (NL2) dots.

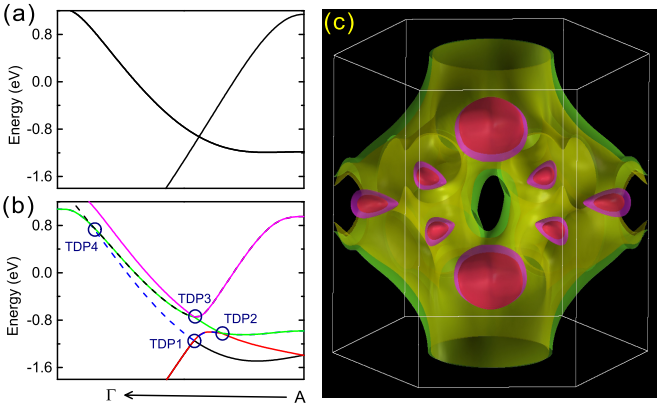

FIG. 4. Band structures along $\Gamma - A$ without (a) and with (b) the SOC. (c) Overview of the Fermi surface of TaS with $E = 0$ eV.

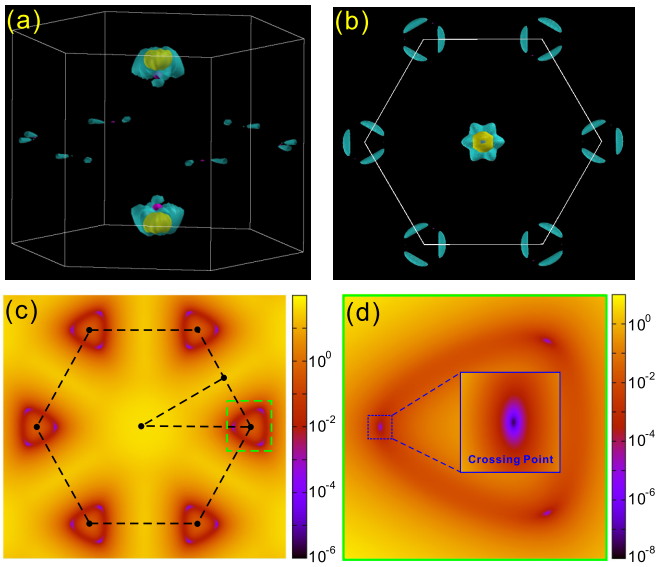

FIG. 5. (a) The overview and (b) the top view of the isoenergy surface at $E = -1.026$ eV. (c) The energy difference between the blue and red bands in Fig. 2 in the $k_z = 0.01006 \times \frac{2\pi}{c}$ plane; the energy difference in the green box is enlarged and demonstrated in panel (d), and the contour box in units of eV indicates that the energy difference at the crossing points is zero.

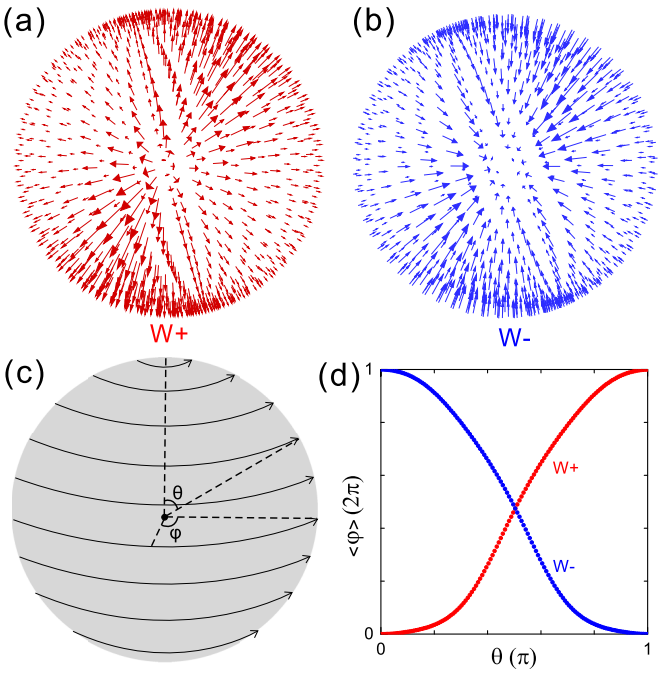

FIG. 6. The Berry curvature around (a) $W+$ and (b) $W-$, respectively. (c) Schematic illustration of the integration paths used to calculate topological charges of Weyl points. (d) Evolution of the Wannier charge centers around the sphere enclosing $W+$ (red) and $W-$ (blue).

C. Weyl nodes

Although the nodal ring preserves around the H point on the $k_z = \pi$ plane, the nodal ring centering at the K point on the $k_z = 0$ plane is fully gapped, and the gapped nodal ring may produce a transition into hidden Weyl points. Generally, it is difficult to identify WPs within momentum space because the WPs are not protected by any additional crystalline symmetry besides the lattice translation and are possibly located at general $\mathbf{k}$ points. However, detailed electronic structure calculations give us some clues. As shown in Figs. 5(a) and 5(b), by tuning the isoenergy reference into the opened gap, one can observe vanishing connections between the threefold rotational symmetric arcs centering at the K point, which indicates that the DOS of the connections becomes zero. However, by further calculations of the energy gap between blue and red bands in Fig. 2(b), we find that the arc connections are simultaneously band crossing points, which are demonstrated in Figs. 5(c) and 5(d). As a consequence, we find six pairs of zero-mass band crossing points off the $k_z = 0$ plane within the gap opened in the original nodal ring, and one pair of typical crossing points is located at $(0.27449, 0.27449, \pm 0.01006)$ in units of reciprocal-lattice vectors marked as $W+$ and $W-$, respectively.

In the following, we will check whether these band crossing points are WPs or not. As an important clue, WPs can be viewed as monopoles with opposite chirality corresponding to the sources and sinks of Berry curvature. Besides, the integral of the Berry curvature on any closed surface in the BZ equals the total chirality of the WPs enclosed by the given surface, which will help us chase down and check WPs quickly. Therefore, to further verify that the connecting points host monopole feature and chirality, we apply the Kubo formula to calculate the Berry curvature by the tight-binding Hamiltonian based on the MLWF [58,59]:

$$\hat{v}_{\alpha(\beta\gamma)} = (i/\hbar)[\hat{H}, \hat{r}_{\alpha(\beta\gamma)}] = \frac{1}{\hbar}\frac{\partial \hat{H}(\mathbf{k})}{\partial k_{\alpha(\beta\gamma)}}, \tag{1}$$

$$\Omega_{n,\alpha\beta}(\mathbf{k}) = -2\,\mathrm{Im}\sum_{m\neq n}\frac{\langle u_{n\mathbf{k}}|\hat{v}_\alpha|u_{m\mathbf{k}}\rangle\langle u_{m\mathbf{k}}|\hat{v}_\beta|u_{n\mathbf{k}}\rangle}{[\omega_m(\mathbf{k}) - \omega_n(\mathbf{k})]^2}, \tag{2}$$

where $\hat{v}_{\alpha(\beta\gamma)}$ is the velocity operator; $\alpha, \beta, \gamma = x, y, z$; $\omega_m(\mathbf{k}) = \varepsilon_n(\mathbf{k})/\hbar$; and $\varepsilon_n(\mathbf{k})$ and $u_{n\mathbf{k}}$ are the eigenvalue and eigenvector of the Hamiltonian $\hat{H}(\mathbf{k})$, respectively. Finally, we obtain the Berry curvature in momentum space for a given band n by

$$\Omega_{n,\gamma}(\mathbf{k}) = \epsilon_{\alpha\beta\gamma}\Omega_{n,\alpha\beta}(\mathbf{k}), \tag{3}$$

where $\epsilon_{\alpha\beta\gamma}$ is the Levi-Civita tensor. By summing over all occupied valence bands, we give the Berry curvature vector $\Omega = (\Omega_x, \Omega_y, \Omega_z)$. Next, we will examine the monopole feature of the crossing points. Since a pair of WPs with opposite chirality represents the source and sink of the Berry curvature, we calculate the Berry curvature distribution in momentum space. From Figs. 6(a) and 6(b), we can clearly see that the Berry curvature around $W+$ and $W-$ is divergent and convergent, respectively, which indicates that $W+$ and $W-$ act as the feature of the source and sink of the Berry curvature.

In order to confirm the chirality of the crossing points, we need to get the flux of Berry curvature through a surface enclosing them. The corresponding flux of Berry curvature is computed by discretizing a closed sphere parametrized by angles θ and φ into 1D loops, as shown in Fig. 6(c).

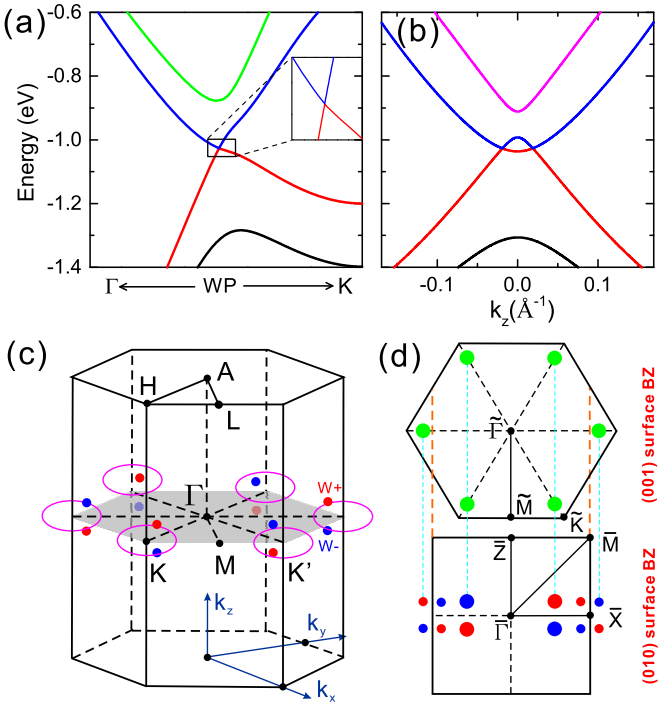

FIG. 7. The detail and overview of the band dispersions around the WPs are demonstrated in panel (a) and panel (b). (c) The original gapless nodal rings in the absence of SOC are denoted by the pink rings, and the emergent WPs in the presence of SOC in the gapped nodal rings are illustrated by the dots, and their chiralities are distinguished by the red (+1) and blue (−1) dots. (d) The projected WPs onto (001) and (010) surfaces, respectively. The green large dots indicate projections of a pair of WPs with opposite chirality, and the chirality becomes indistinguishable. The red and blue large dots indicate two projected WPs with the same chirality, while the small dots indicate the single projected WP.

Then, we calculate the WCCs on longitudinal loops around a sphere enclosing the crossing point. The sum of the WCCs on a loop $\mathcal{C}$ with longitudinal θ angle corresponds to the accumulated Berry phase along the loop, or equal to the average position $\langle\varphi\rangle$ of the charge on the loop. It can be determined from the Wilson loop $\mathcal{W}(\mathcal{C})$ as

$$\varphi(\theta)=\mathrm{Im}\{\ln[\det \mathcal{W}(\mathcal{C})]\}, \tag{4}$$

where $\mathcal{W}(\mathcal{C})=\prod_{i=0}^{L-1} M^{(\mathbf{k}_i,\mathbf{k}_{i+1})}$ and $[M^{(\mathbf{k}_i,\mathbf{k}_{i+1})}]_{mn}=\langle u_{m\mathbf{k}_i}|u_{n\mathbf{k}_{i+1}}\rangle$ are the overlap matrices along the loop $\mathcal{C}$. Since 1D loops cover a closed surface, the center of charge $\langle\varphi\rangle$ can only shift by an integer multiple of 2π when θ varies from zero to π. This multiple is equal to the chirality $\mathcal{C}$ of the crossing point enclosed in the sphere. Therefore, we apply the method to a sphere enclosing $W+$ or $W-$. As shown in Fig. 6(d), when the angle θ varies from zero to π, the average position of the Wannier centers $\langle\varphi\rangle$ is shifted by 2π or -2π, which indicates that $W+$ and $W-$ are indeed a pair of WPs with chirality $\mathcal{C}=+1$ and -1, respectively.

Around the WPs ($W+$ and $W-$), we plot the energy dispersions, as shown in Figs. 7(a) and 7(b). TaS hosts high-symmetry D_{3h} including C_3 rotation and mirror symmetry, etc., which results in all WPs being located at the same energy (1.026 eV below the Fermi level). By utilizing the above comprehensive techniques, we obtain at once the positions and chirality of all six pairs of WPs in the first whole BZ, which are clearly presented in Fig. 7(c). All these WPs are located near the K point and its time-reversal K' point and are off the $k_z=0$ mirror plane. Figure 7(d) displays the projection of all WPs onto the top and side surfaces. When these WPs are projected onto the top (001) surface, each pair of WPs with opposite chirality is projected onto the same position labeled by large green dots, whereas on the protected (010) surface the WPs with different chirality are projected onto a different position. The large and small dots represent the projections of two WPs with same chirality and a single WP, respectively.

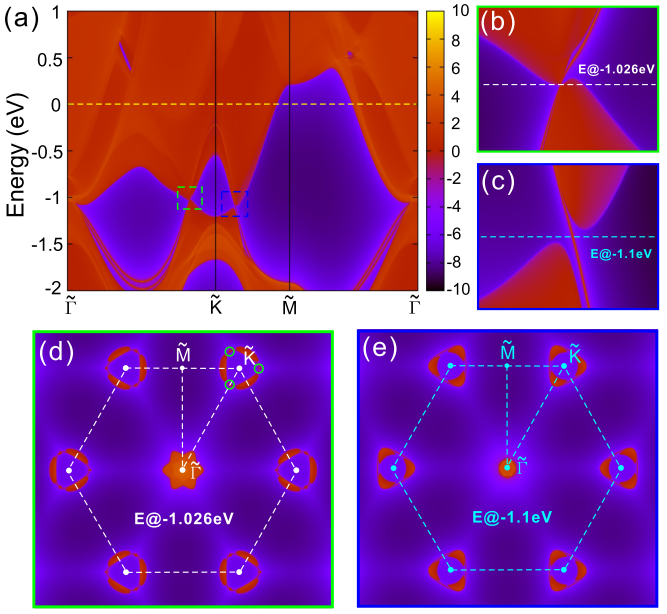

FIG. 8. (a) The projected surface density of states for the (001) surface. (b), (c) The enlarged surface states in panel (a). (d), (e) The Fermi surface of the projected (001) surface in the whole BZ with $E=-1.026$ and -1.1 eV, respectively.

D. Surface states and Fermi arcs

Since different projections bring different expressions of chirality of WPs, we calculate the projected surface states and Fermi surfaces (Fermi arcs) onto the (001) and (010) surfaces. The (001) surface states and Fermi surfaces are shown in Fig. 8. Around the $\tilde{K}$ point, there is a analogous nodal ring but with a bulk gap about 30 meV due to the spin-orbit interaction along the $\tilde{K}-\tilde{M}$ direction, as shown in Fig. 8(c). In Fig. 8(b), a Weyl node is exactly located at -1.026 eV on the $\tilde{\Gamma}-\tilde{K}$ line, which is mainly rooted in the contribution of the projected WP. Around the symmetric $\tilde{K}$ or $\tilde{K}'$ point in the BZ, there are three pairs of projected WPs existing, which will generate threadlike Fermi arcs, as clearly presented in Fig. 8(d). Each green circle represents the projections of two WPs with opposite chirality, which interconnect by the Fermi arcs. Moreover, since the TDPs are located on the $\Gamma-A$ line, they are projected on the $\tilde{\Gamma}$ point surrounded by the bulk state projections.

The (010) surface states and Fermi surfaces are presented in Fig. 9. From Fig. 9(a), one can clearly see that there is a

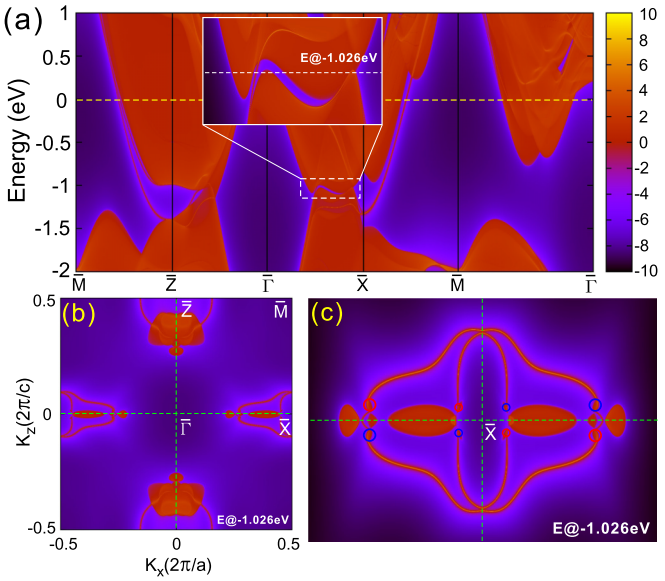

FIG. 9. (a) The projected surface density of states for the (010) surface. (b) The Fermi surface of the projected (010) surface with $E = -1.026$ eV. The Fermi surface around the $\bar{X}$ point in panel (b) is enlarged in panel (c), and where the projected WPs carrying opposite chirality are indicated by the red and blue circles, respectively.

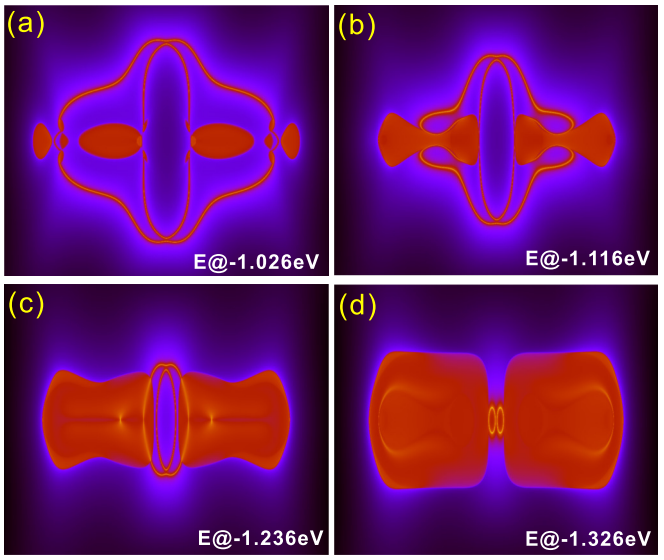

FIG. 10. (b) The evolution of the isoenergy surface contours around the $\bar{X}$ point of the projected (010) surface with respect to the chemical potentials is demonstrated at (a) $E = -1.026$ eV, (b) $E = -1.116$ eV, (c) $E = -1.236$ eV, and (d) $E = -1.326$ eV.

surface Dirac cone at the $\bar{Z}$ point, which is a result of $Z_2 = 1$ of the $k_z = \pi$ plane. The two branches of the surface Dirac cone connect the bulk states of the conduction and valence bands, respectively. In order to observe the fancy Fermi arcs, we plot the Fermi surface at $E = -1.026$ eV, as shown in Figs. 9(b) and 9(c). In Fig. 9(c), the projected WPs and Fermi arcs are clearly presented, and each Fermi arc connects the projections of the WPs with opposite chirality. The red and blue large circles represent the projections of two WPs with the same chirality and have a monopole charge $+2$ and -2, respectively, while the red and blue small circles represent a single projected WP and have a monopole charge $+1$ and -1, respectively. This is consistent with the description of Fig. 7(d). In addition, the TDPs located at the $\Gamma - A$ line in the bulk band are projected onto the $\bar{\Gamma} - \bar{Z}$ path, and they cannot be detached from other surface states and are buried in the projected bulk states, which is mainly due to the breaking of the C_3 and vertical mirror plane σ_v symmetry on the (010) side surface.

E. Lifshitz transition

Since the connections between WPs carrying opposite chirality are preserved on the (010) projection surface, and each pair of different chiral WPs is located very close to each other in momentum space, they can inevitably hybridize together. By adjusting chemical potential appropriately, one can expect a topological change in the band contours, which is known as the Lifshitz transition [60–63]. In Fig. 10, we present the Lifshitz transition by changing the contour energy. At $E = -1.026$ eV, Fermi arcs connecting the projected WPs with opposite chirality are clearly shown in Fig. 10(a), which has been introduced in detail above. As the contour energy decreases, the Fermi arcs disappear and the topological properties will change. The projected surface bands will close to each other, then form two concentric ellipses, and finally develop into two ellipses side by side.

IV. SUMMARY AND CONCLUSIONS

In conclusion, in this paper we report that TaS is a stable topological metal hosting versatile quasiparticle excitations such as topological nodal rings, Weyl points, and threefold degenerate points protected by the rotation symmetry C_3 and vertical mirror symmetry σ_v simultaneously in the presence of SOC. Based on the DFT calculations, we study the topologically nontrivial properties in TaS both in bulk states and projected surface states. We find that the nodal ring centering at the H point of momentum space remains closed to meet the requirement of the horizontal mirror symmetry σ_h and the nodal ring centering at the K point is fully gapped by introducing the SOC. In the gapped nodal ring, there are six pairs of WPs associating with the point group D_{3h} and locating at the same energy in the first BZ. Chirality and monopole features of the WPs are verified by the calculation of the Berry curvature, and the characteristic Fermi arcs are found on the particular projected surfaces, which connects the projections of WPs with opposite chirality. By the projection onto the (010) surface and adjustment of chemical potential, a Lifshitz transition is also observed. The coexistence of versatile topological excitations brings extraordinary properties such as drumhead surface states and negative magnetoresistance effects. In light of these properties of the electronic band structures and surface states in TaS, we provide a guiding principle to search for the particular topological semimetal, and establish an experimentally achievable material platform for studying unique topological phenomena in solids.

ACKNOWLEDGMENTS

This work was supported by National Natural Science Foundation of China Grant No. 11504366 and National Basic Research Program of China Grants No. 2015CB921503 and No. 2016YFE0110000.

[1] M. Z. Hasan and C. L. Kane, Rev. Mod. Phys. **82**, 3045 (2010).
[2] X.-L. Qi and S.-C. Zhang, Phys. Today **63**, 33 (2010).
[3] J. E. Moore, Nature (London) **464**, 194 (2010).
[4] X.-L. Qi and S.-C. Zhang, Rev. Mod. Phys. **83**, 1057 (2011).
[5] C. Herring, Phys. Rev. **52**, 365 (1937).
[6] G. E. Volovik, Proc. Natl. Acad. Sci. USA **96**, 6042 (1999).
[7] X. Wan, A. M. Turner, A. Vishwanath, and S. Y. Savrasov, Phys. Rev. B **83**, 205101 (2011).
[8] S. M. Young, S. Zaheer, J. C. Y. Teo, C. L. Kane, E. J. Mele, and A. M. Rappe, Phys. Rev. Lett. **108**, 140405 (2012).
[9] S. M. Young and C. L. Kane, Phys. Rev. Lett. **115**, 126803 (2015).
[10] Z. Wang, Y. Sun, X.-Q. Chen, C. Franchini, G. Xu, H. Weng, X. Dai, and Z. Fang, Phys. Rev. B **85**, 195320 (2012).
[11] B. J. Wieder, Y. Kim, A. M. Rappe, and C. L. Kane, Phys. Rev. Lett. **116**, 186402 (2016).
[12] A. A. Burkov, M. D. Hook, and L. Balents, Phys. Rev. B **84**, 235126 (2011).
[13] R. Yu, H. Weng, Z. Fang, X. Dai, and X. Hu, Phys. Rev. Lett. **115**, 036807 (2015).
[14] Y. Kim, B. J. Wieder, C. L. Kane, and A. M. Rappe, Phys. Rev. Lett. **115**, 036806 (2015).
[15] C. Fang, Y. Chen, H.-Y. Kee, and L. Fu, Phys. Rev. B **92**, 081201 (2015).
[16] K. Mullen, B. Uchoa, and D. T. Glatzhofer, Phys. Rev. Lett. **115**, 026403 (2015).
[17] G. Bian, T.-R. Chang, R. Sankar, S.-Y. Xu, H. Zheng, T. Neupert, C.-K. Chiu, S.-M. Huang, G. Chang, I. Belopolski, D. S. Sanchez, M. Neupane, N. Alidoust, C. Liu, B. Wang, C.-C. Lee, H.-T. Jeng, C. Zhang, Z. Yuan, S. Jia, A. Bansil, F. Chou, H. Lin, and M. Z. Hasan, Nat. Commun. **7**, 10556 (2016).
[18] G. Bian, T.-R. Chang, H. Zheng, S. Velury, S.-Y. Xu, T. Neupert, C.-K. Chiu, S.-M. Huang, D. S. Sanchez, I. Belopolski, N. Alidoust, P.-J. Chen, G. Chang, A. Bansil, H.-T. Jeng, H. Lin, and M. Z. Hasan, Phys. Rev. B **93**, 121113 (2016).
[19] Y.-H. Chan, C.-K. Chiu, M. Y. Chou, and A. P. Schnyder, Phys. Rev. B **93**, 205132 (2016).
[20] D. Takane, Z. Wang, S. Souma, K. Nakayama, C. X. Trang, T. Sato, T. Takahashi, and Y. Ando, Phys. Rev. B **94**, 121108 (2016).
[21] H. Huang, J. Liu, D. Vanderbilt, and W. Duan, Phys. Rev. B **93**, 201114 (2016).
[22] Z. Zhu, M. Li, and J. Li, Phys. Rev. B **94**, 155121 (2016).
[23] J.-P. Sun, D. Zhang, and K. Chang, Chin. Phys. Lett. **34**, 027102 (2017).
[24] A. A. Burkov and L. Balents, Phys. Rev. Lett. **107**, 127205 (2011).
[25] G. B. Halász and L. Balents, Phys. Rev. B **85**, 035103 (2012).
[26] H. Weng, C. Fang, Z. Fang, B. A. Bernevig, and X. Dai, Phys. Rev. X **5**, 011029 (2015).
[27] S.-Y. Xu, I. Belopolski, N. Alidoust, M. Neupane, G. Bian, C. Zhang, R. Sankar, G. Chang, Z. Yuan, C.-C. Lee, S.-M. Huang, H. Zheng, J. Ma, D. S. Sanchez, B. Wang, A. Bansil, F. Chou, P. P. Shibayev, H. Lin, S. Jia, and M. Z. Hasan, Science **349**, 613 (2015).
[28] Y. Sun, S.-C. Wu, M. N. Ali, C. Felser, and B. Yan, Phys. Rev. B **92**, 161107 (2015).
[29] G. Autès, D. Gresch, M. Troyer, A. A. Soluyanov, and O. V. Yazyev, Phys. Rev. Lett. **117**, 066402 (2016).
[30] J. Sánchez-Barriga, M. G. Vergniory, D. Evtushinsky, I. Aguilera, A. Varykhalov, S. Blügel, and O. Rader, Phys. Rev. B **94**, 161401 (2016).
[31] K. Deng, G. Wan, P. Deng, K. Zhang, S. Ding, E. Wang, M. Yan, H. Huang, H. Zhang, Zhilin, J. Denlinger, A. Fedorov, H. Yang, W. Duan, H. Yao, Y. Wu, S. Fan, H. Zhang, X. Chen, and S. Zhou, Nat. Phys. **12**, 1105 (2016).
[32] A. Tamai, Q. S. Wu, I. Cucchi, F. Y. Bruno, S. Riccò, T. K. Kim, M. Hoesch, C. Barreteau, E. Giannini, C. Besnard, A. A. Soluyanov, and F. Baumberger, Phys. Rev. X **6**, 031021 (2016).
[33] B. Bradlyn, J. Cano, Z. Wang, M. G. Vergniory, C. Felser, R. J. Cava, and B. A. Bernevig, Science **353**, aaf5037 (2016).
[34] Z. Zhu, G. W. Winkler, Q. S. Wu, J. Li, and A. A. Soluyanov, Phys. Rev. X **6**, 031003 (2016).
[35] H. Weng, C. Fang, Z. Fang, and X. Dai, Phys. Rev. B **94**, 165201 (2016).
[36] G. W. Winkler, Q. S. Wu, M. Troyer, P. Krogstrup, and A. A. Soluyanov, Phys. Rev. Lett. **117**, 076403 (2016).
[37] S. Zaheer, S. M. Young, D. Cellucci, J. C. Y. Teo, C. L. Kane, E. J. Mele, and A. M. Rappe, Phys. Rev. B **87**, 045202 (2013).
[38] S. A. Yang, H. Pan, and F. Zhang, Phys. Rev. Lett. **113**, 046401 (2014).
[39] V. K. Slovyanskikh and N. T. Kuznetsov, Russ. J. Inorg. Chem. **29**, 1088 (1984).
[40] A. Friedrich, W. Morgenroth, L. Bayarjargal, E. A. Juarez-Arellano, B. Winkler, and Z. Konôpková, High Press. Res. **33**, 633 (2013).
[41] L. Litinskii, Solid State Commun. **71**, 299 (1989).
[42] L. Litinskii, Solid State Commun. **75**, 1009 (1990).
[43] G. Örlygsson and B. Harbrecht, J. Am. Chem. Soc. **123**, 4168 (2001).
[44] K. Parlinski, Z. Q. Li, and Y. Kawazoe, Phys. Rev. Lett. **78**, 4063 (1997).
[45] A. Togo, F. Oba, and I. Tanaka, Phys. Rev. B **78**, 134106 (2008).
[46] G. Kresse and J. Furthmüller, Phys. Rev. B **54**, 11169 (1996).
[47] J. P. Perdew, K. Burke, and M. Ernzerhof, Phys. Rev. Lett. **77**, 3865 (1996).
[48] P. E. Blöchl, Phys. Rev. B **50**, 17953 (1994).
[49] H. J. Monkhorst and J. D. Pack, Phys. Rev. B **13**, 5188 (1976).
[50] N. Marzari and D. Vanderbilt, Phys. Rev. B **56**, 12847 (1997).
[51] I. Souza, N. Marzari, and D. Vanderbilt, Phys. Rev. B **65**, 035109 (2001).
[52] M. P. L. Sancho, J. M. L. Sancho, and J. Rubio, J. Phys. F **14**, 1205 (1984).

[53] M. P. L. Sancho, J. M. L. Sancho, J. M. L. Sancho, and J. Rubio, J. Phys. F **15**, 851 (1985).
[54] Q. Wu, S. Zhang, H.-F. Song, M. Troyer, and A. A. Soluyanov, arXiv:1703.07789.
[55] A. A. Soluyanov and D. Vanderbilt, Phys. Rev. B **83**, 235401 (2011).
[56] A. A. Soluyanov and D. Vanderbilt, Phys. Rev. B **83**, 035108 (2011).
[57] M. Taherinejad, K. F. Garrity, and D. Vanderbilt, Phys. Rev. B **89**, 115102 (2014).
[58] D. Xiao, M.-C. Chang, and Q. Niu, Rev. Mod. Phys. **82**, 1959 (2010).
[59] X. Wang, J. R. Yates, I. Souza, and D. Vanderbilt, Phys. Rev. B **74**, 195118 (2006).
[60] Y. Wu, N. H. Jo, M. Ochi, L. Huang, D. Mou, S. L. Bud'ko, P. C. Canfield, N. Trivedi, R. Arita, and A. Kaminski, Phys. Rev. Lett. **115**, 166602 (2015).
[61] S.-Y. Xu, C. Liu, I. Belopolski, S. K. Kushwaha, R. Sankar, J. W. Krizan, T.-R. Chang, C. M. Polley, J. Adell, T. Balasubramanian, K. Miyamoto, N. Alidoust, G. Bian, M. Neupane, H.-T. Jeng, C.-Y. Huang, W.-F. Tsai, T. Okuda, A. Bansil, F. C. Chou, R. J. Cava, H. Lin, and M. Z. Hasan, Phys. Rev. B **92**, 075115 (2015).
[62] G. E. Volovik, Low Temp. Phys. **43**, 47 (2017).
[63] K. Zhang and G. Volovik, arXiv:1604.00849.